Front. Phys. 12(1), 124201 (2017)
DOI 10.1007/s11467-016-0601-6

RESEARCH ARTICLE

Fundamental modes in waveguide pipe twisted by saturated double-well potential

Gui-Hua Chen[1], Hong-Cheng Wang[1,*], Zhao-Pin Chen[2], Yan Liu[3,†]

[1] *Department of Electronic Engineering, Dongguan University of Technology, Dongguan 523808, China*
[2] *Department of Physical Electronics, School of Electrical Engineering, Faculty of Engineering, Tel Aviv University, Tel Aviv IL-69978, Israel*
[3] *Department of Applied Physics, South China Agricultural University, Guangzhou 510642, China*
*Corresponding authors. Email: *hcwang@126.com, †lycalm@scau.edu.cn*
Received April 5, 2016; accepted June 9, 2016

We study fundamental modes trapped in a rotating ring with a saturated nonlinear double-well potential. This model, which is based on the nonlinear Schrödinger equation, can be constructed in a twisted waveguide pipe in terms of light propagation, or in a Bose–Einstein condensate (BEC) loaded into a toroidal trap under a combination of a rotating π-out-of-phase linear potential and nonlinear pseudopotential induced by means of a rotating optical field and the Feshbach resonance. Three types of fundamental modes are identified in this model, one symmetric and the other two asymmetric. The shape and stability of the modes and the transitions between different modes are investigated in the first rotational Brillouin zone. A similar model used a Kerr medium to build its nonlinear potential, but we replace it with a saturated nonlinear medium. The model exhibits not only symmetry breaking, but also symmetry recovery. A specific type of unstable asymmetric mode is also found, and the evolution of the unstable asymmetric mode features Josephson oscillation between two linear wells. By considering the model as a configuration of a BEC system, the ground state mode is identified among these three types, which characterize a specific distribution of the BEC atoms around the trap.

Keywords Twisted double-well waveguide, saturated nonlinear potential, symmetry breaking, symmetry recovery

PACS numbers 42.65.Tg, 03.75.Lm, 47.20.Kv, 05.45.Yv

Frontiers of Physics

1 Introduction

Nonlinear media exhibiting nonlinearities such as Kerr [1–3], saturable [4, 5], and quadratic nonlinearities [6], and even nonlocal nonlinear media [8, 9], play a dominant role in light manipulation and can be used to form many types of nonhomogeneous landscapes such as waveguide arrays and photonic crystals. One important structure for light manipulation, which is implemented using linear and nonlinear media, is the periodic lattice. Wave evolution in a combination of both linear and nonlinear periodic lattices exhibits many dynamics [10–13]. A light wave guided along the lattices in the paraxial approximation obeys the nonlinear Schrödinger equation (NLSE), in which the linear and nonlinear lattices are represented separately by a usual periodic potential and a periodic pseudopotential. Moreover, the Bose–Einstein condensate (BEC), an ideal test platform for nonlinear science, has been the subject of intense attention and research, which has revealed many novel modes [14–16]. The formulation of this model can be changed directly into the form of the Gross–Pitaevskii equation under the mean-field approximation and can be used to discuss matter waves in a BEC that is trapped in a combination of both a linear periodic potential created by an optical or magnetic lattice, and a pseudopotential, which may be induced by periodic modulation of the local nonlinearity provided by properly patterned optical or magnetic fields [17–21].

Several works in the past decade have considered a special combination of linear and nonlinear lattices, in which the maxima of the refractive index coincide with the minima of the local strength of the self-focusing nonlinearity

and vice versa [22–29]. This medium, which features a competing π-out-of-phase juxtaposed linear potential and nonlinear pseudopotential, may naturally be called an inverted nonlinear photonic crystal (INPC). INPCs reportedly can be fabricated using a technique based on direct laser writing in silica [30, 31]. It was also predicted that a similar setting could be created in a virtual form using an electromagnetically induced transparency acting on dopant atoms periodically distributed in a passive matrix [25, 28, 32–34]. Owing to competition between the linear and nonlinear lattices, solitons in INPCs may feature specific power-dependent properties, such as double symmetry breaking [23]. Very recently, it was reported that a twisted waveguide pipe, which possesses an inverted nonlinear double-well potential, can support the existence of three types of fundamental modes [29]. This work found that symmetry breaking among these modes could exhibit properties different from those found in the usual nonlinear rotating double-well system [35–41]. Such previous studies on INPCs deal with a system possessing both linear and Kerr (cubic) nonlinear potentials. However, in the counterpart containing only a saturable nonlinearity, INPCs not only naturally embody the inverted restriction of both the linear and Kerr nonlinear potentials if the total power of the field is small (as mentioned below), but also can intrinsically feature different types of power-dependent properties. It has been reported that solitary waves in such types of INPCs are compactons [24], which switch their center between the linear and nonlinear segments when the total power of the waves varies.

In this work, we study the fundamental modes trapped in a twisted cylindrical-shell waveguide (i.e., a waveguide pipe) carrying a saturated nonlinear double-well potential. To analyze the basic characteristics of this system, we use a one-dimensional NLSE with a potential rotating at a rate of ω. The waveguide pipe, with a double-well surface structure written into the material of the shell, may be realized by experimental methods in which an SU-8 polymer (a commonly used transparent negative photoresist) is doped by Rhodamine B (RhB, a dye featuring saturable absorption) in the form of $V(\theta)$ [42–45]. The rotation is established by twisting the waveguide pipe with a pitch of $2\pi/\omega$; then azimuthal modulation of the potential is written into the material of the shell in the form of $V(\theta-\omega z)$.

The paper is structured as follows: In Section 2, we build the model, formulate the corresponding system, and present the analytic technique for determining the stability of the modes. The numerical results for stable fundamental modes in the model are presented in Section 3. We discuss and analyze the transitions, symmetry breaking, and symmetry recovery between modes in this section. In Section 4, we present our conclusion.

2 The model

As discussed above, we establish a twisted cylindrical-shell waveguide with a saturated nonlinear double-well potential $V(\theta-\omega z) = Acos^2(\theta-\omega z)$. Here, A is the amplitude of the nonlinear potential. The propagation dynamics of a probe wave within the waveguide can be described by the underlying 1D scaled nonlinear Schrödinger equation,

$$\mathrm{i}\frac{\mathrm{d}}{\mathrm{d}z}\psi = \left[-\frac{1}{2r_0}\frac{\mathrm{d}^2}{\mathrm{d}\theta^2} + \frac{\sigma V(\theta-\omega z)}{1+|\psi|^2}\right]\psi, \tag{1}$$

where r_0, which can be fixed at 1, is the radius of the cylindrical-shell waveguide, ω is the rotation speed of the potential, and σ is the nonlinear parameter. $\sigma = -1/1$ represents the self-focusing/defocusing nonlinearity. When we replace θ with $\theta' = \theta-\omega z$, the equation can be rewritten as

$$\mathrm{i}\frac{\mathrm{d}}{\mathrm{d}z}\psi = \left[-\frac{1}{2}\frac{\mathrm{d}^2}{\mathrm{d}\theta'^2} + \mathrm{i}\omega\frac{\mathrm{d}}{\mathrm{d}\theta'} + \frac{\sigma V(\theta')}{1+|\psi|^2}\right]\psi. \tag{2}$$

For a narrow toroidal BEC trapped in a rotating potential, the corresponding Gross-Pitaevskii equation written in the rotating reference frame is different from Eq. (2), with the propagation distance z replaced by t. Stationary modes with a real propagation constant $-\mu$ (for a BEC, $-\mu$ is regarded as the chemical potential) can be found as $\psi(\theta',z) = \phi(\theta')\mathrm{e}^{-\mathrm{i}\mu z}$, where $\phi(\theta')$, a complex function, satisfies the following equation:

$$\left[-\frac{1}{2}\frac{\mathrm{d}^2}{\mathrm{d}\theta'^2} + \mathrm{i}\omega\frac{\mathrm{d}}{\mathrm{d}\theta'} + \frac{\sigma V(\theta')}{1+|\phi|^2}\right]\phi = \mu\phi. \tag{3}$$

Further, Eq. (2) conserves the total power (norm) of the field:

$$P = \int_{-\pi}^{\pi}|\psi(\theta')|^2\mathrm{d}\theta'. \tag{4}$$

The periodic boundary condition, $V(\theta'+2\pi) = V(\theta')$ and $\psi(\theta'+2\pi) = \psi(\theta')$, makes Eq. (2) invariant with respect to the *boost transformation*, which allows one to change the rotation speed from ω to $\omega - N$ for an arbitrary integer N:

$$\psi(\theta',z;\omega-N) = \psi(\theta',z;\omega)\exp\left[-\mathrm{i}N\theta' + \mathrm{i}\left(\frac{1}{2}N^2 - N\omega\right)z\right]; \tag{5}$$

hence, the rotation speed may be restricted to the interval $0 \le \omega < 1$. Furthermore, Eq. (2) also admits an additional invariance, relating solutions with opposite signs of the speed: $\psi(\theta',z;\omega) = \psi^*(\theta',-z;-\omega)$. Combined with the shift $\omega \to \omega+1$, the latter transformation

demonstrates that the solutions for the rotation speeds ω and $1-\omega$ (for $0 \le \omega \le 1/2$) are equal to each other. Therefore, the speed of rotation can further be restricted to a smaller interval,

$$0 \le \omega \le \frac{1}{2}, \tag{6}$$

which is the so-called first rotational Brillouin zone.

The stability of the stationary modes is investigated through numerical computation of eigenvalues and demonstrated by a real-time simulation with infinitesimal perturbation. The perturbed solutions are imported as the usual form,

$$\psi = \mathrm{e}^{-\mathrm{i}\mu z}[\phi(\theta') + u(\theta')\mathrm{e}^{\mathrm{i}\lambda z} + v^*(\theta')\mathrm{e}^{-\mathrm{i}\lambda^* z}], \tag{7}$$

where $u(\theta')$ and $v(\theta')$ are the perturbation eigenmodes, and λ is the corresponding eigenfrequency. Substituting Eq. (7) into Eq. (2) and applying linearization, it becomes a linear eigenvalue problem,

$$\begin{pmatrix} \mu - \hat{H} - \mathrm{i}\omega\dfrac{\mathrm{d}}{\mathrm{d}\theta'} & -\dfrac{\sigma V}{F^2}\phi^2 \\ -\dfrac{\sigma V}{F^2}\phi^{*2} & -\mu + \hat{H} - \mathrm{i}\omega\dfrac{\mathrm{d}}{\mathrm{d}\theta'} \end{pmatrix} \begin{pmatrix} u \\ v \end{pmatrix} = \lambda \begin{pmatrix} u \\ v \end{pmatrix}, \tag{8}$$

where $\hat{H} = -(1/2)\mathrm{d}^2/\mathrm{d}\theta'^2 + \sigma V/F^2$ is the single-particle Hamiltonian, and $F = 1 + |\phi|^2$. The underlying solution ϕ is stable if all the eigenvalues λ are real.

In our model, when the total power of the field is low, the linear and nonlinear potentials, denoted as $V_L(\theta') = \sigma V(\theta')$ and $V_N(\theta') = -\sigma V(\theta')$, respectively, are π-out-of-phase juxtaposed, which can be determined by polynomial expansion of the last term in Eq. (2) and retention of the first two items, $\sigma V(\theta')\psi$ and $-\sigma V(\theta')|\psi|^2\psi$. For a linear potential, two maxima appear at $\theta' = 0$ and $-\pi$ (if the potential domain is set to $-\pi \le \theta' < \pi$), and the two minima appear at $\theta' = -\pi/2$ and $\pi/2$. In contrast, for a nonlinear potential, the maxima appear at $\theta' = -\pi/2$ and $\pi/2$, whereas the two minima appear at $\theta' = -\pi$ and 0. As the regions close to the minima of linear or nonlinear potentials dominate the linear or nonlinear propagation dynamics of the probe wave, respectively, we divide the potential domain into four segments: $[-3\pi/4, -\pi/4)$, $[\pi/4, 3\pi/4)$, $[-\pi/4, \pi/4)$, and $[-\pi, -3\pi/4) \cup [3\pi/4, \pi)$ (which is equivalent to $[3\pi/4, 5\pi/4)$ for the periodic boundary condition). The former two segments are called linear segments to indicate that the linear effect in these areas is stronger than the nonlinear one. In the latter two segments, which are called nonlinear segments, the nonlinear effect is stronger than the linear one. Depending on the distribution of the linear and nonlinear areas, there are two symmetric axes in the cross section of the twisted waveguide pipe. One crosses $-\pi/2$ and $\pi/2$, whereas the other passes through $-\pi$ and π. Figure 1 shows a sketch of the twisted waveguide pipe and its cross section.

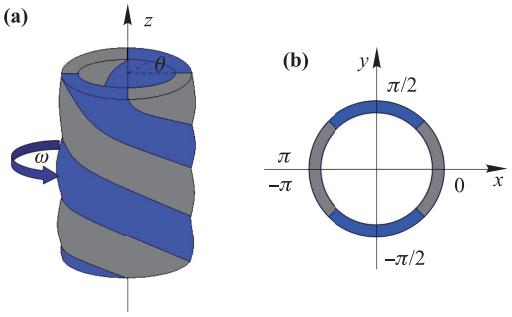

Fig. 1 **(a)** The air-core cylindrical waveguide pipe, twisted by saturated nonlinear potentials with a rotating speed ω. The blue belts represent the linear segments, while the gray ones indicate the nonlinear segments. **(b)** Cross-section of the waveguide pipe: two symmetric axes, labeled x and y, cross the linear and nonlinear segments, respectively.

3 Results and discussion

Stationary fundamental solutions to Eq. (3) are obtained via the imaginary-time propagation (ITP) method [46, 47]. Three types of fundamental modes are found in this model. One mode is symmetric, and the other two are asymmetric. Both types are identified in the domain $-\pi \le \theta' < \pi$ with different inputs, which are listed in Tab. 1 and denoted as SY, ASY-I, and ASY-II, respectively. Typical examples of stable solutions for each mode with a set of parameters (A, ω, P) are shown in Fig. 2.

In the SY mode, there are two peaks in the intensity profile centered on $\theta' = -\pi/2$ and $\theta' = \pi/2$ (the two minima of the linear potential V_L). Further, for the ASY-II mode, there is only one peak left over in the intensity profile, the center of which is located at $\theta' = -\pi/2$ or $\pi/2$ [the center of the peak in Fig. 2(c2) is located at $\theta' = \pi/2$]. However, the intensity profile of the ASY-I mode is slightly complicated. One or two peaks located around $\theta' = 0$ appear in the intensity profile depending on the power of the probe wave. Note that $\theta' = 0$ is one

Table 1 Different species of stable fundamental modes, labeled by input waveforms which generate them.

Types of fundamental modes	Inputs
Fundamental symmetry (SY)	$\sin^2\theta'$
Fundamental asymmetry I (ASY-I)	$1+\cos\theta'$
Fundamental asymmetry II (ASY-II)	$1+\sin\theta'$

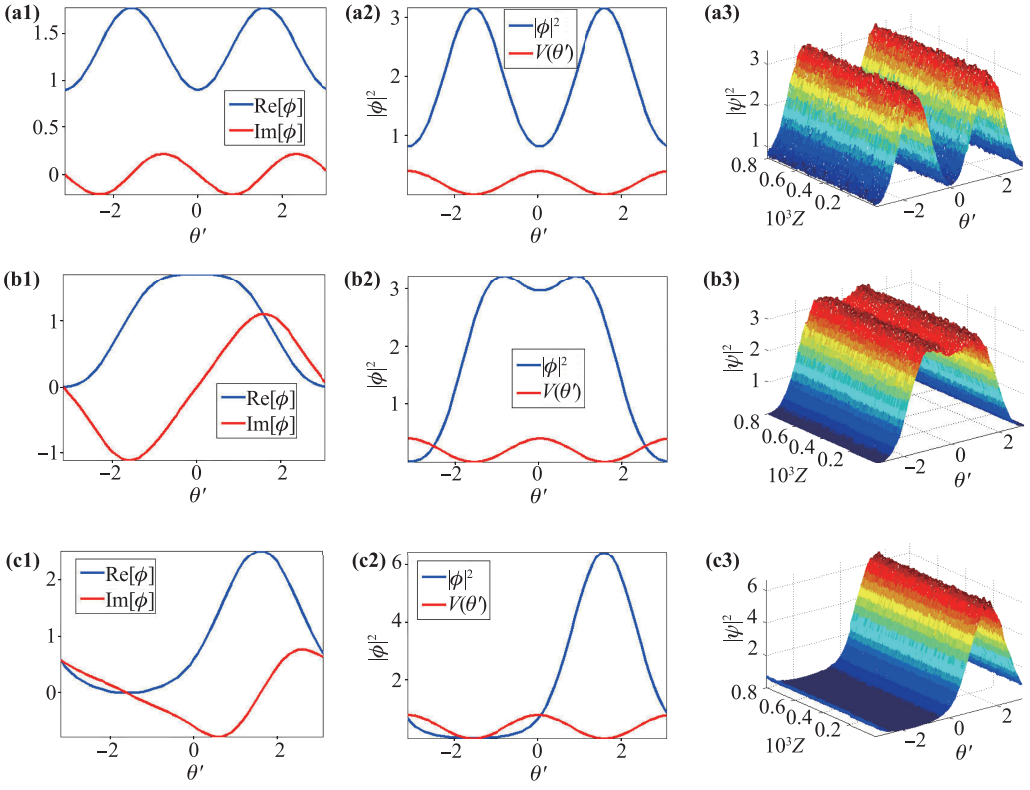

Fig. 2 Examples of stable fundamental modes with a set of parameter $(V, P, \omega) = (2, 12, 0.5)$. Panels **(a1)**, **(b1)**, and **(c1)** represent the real and imaginary parts of SY, ASY-I, and ASY-II, respectively. Panels **(a2)**, **(b2)**, and **(c2)** exhibit the intensity profiles of the same modes. The red curves in these panels depict the modulation of $V(\theta')$, which in this case coincides with the shape of $\cos^2\theta'$. Panels **(a3)**, **(b3)**, and **(c3)** demonstrate the direct simulations (real-time evolution with perturbation by noise to the solution) of these modes.

of the minima of the nonlinear potential V_N. Obviously, there is more power distributed around the minima of the linear potential for both the SY and ASY-II modes, whereas the ASY-I mode has more power near the minima of the nonlinear potential.

The shape of the fundamental modes varies with the total power of the probe wave P. To study the effect of P on the shape, the SY and ASY-I modes are numerically simulated, and their shapes are depicted for a normalized strength. The variation in the shapes of the SY and ASY-I modes for different P are shown in Fig. 3 (the shape variation of the ASY-II mode is not shown here, as this type of mode exists stably only in the lower-power region). For the SY mode, the power tends to appear at the centers of the two peaks with increasing P, whereas for the ASY-I mode, the energy gradually focuses on the location of $\theta' = 0$.

To study the existence and stability of the modes and the transitions between modes, we calculated the distribution of stable fundamental modes with different amplitudes A in the (P, ω) plane (Fig. 4). Different colors indicate diverse regions in which one or more different modes are stable. The meanings of the colors are listed

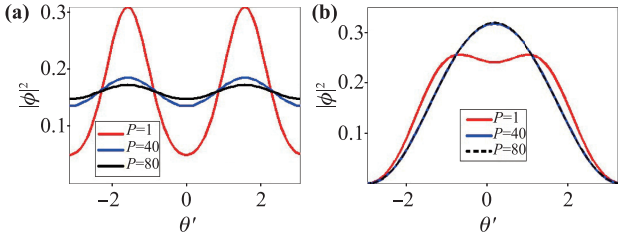

Fig. 3 The intensity distribution of the SY and ASY-I modes varied with $P(P = 1, 40, 80)$, in a normalized strength, $|\phi|^2 = |\psi|^2/P$. The set of parameters are $(A, \omega) = (2, 0)$ for panel **(a)** and $(A, \omega) = (0.5, 0.5)$ for panel **(b)**. Noted that the intensity curves with $P = 40$ and 80 in panel (b) coincide with each other.

in Tab. 2. These results clearly show that the rotation speed ω and amplitude A of the potential play important roles in the distribution of stable fundamental modes. Note that the saturation effect of the nonlinear potential could be neglected, as P is sufficiently large. Equivalently, the nonlinear effect is notable only in the region with a lower power P. By examining the distribution

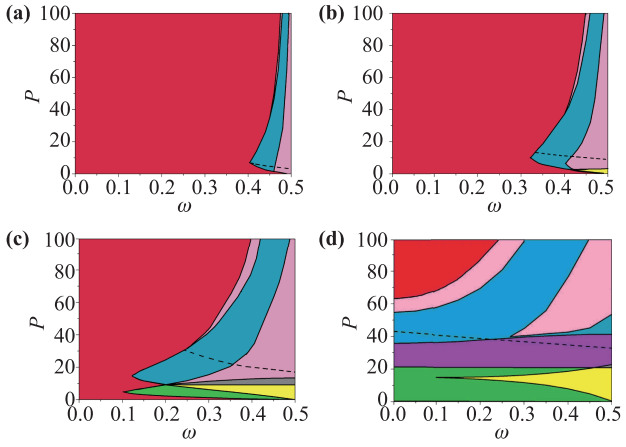

Fig. 4 The distribution diagram of stable modes in the (P,ω) plane with **(a)** $A=0.5$; **(b)** $A=1$; **(c)** $A=2$ and **(d)** $A=4$. The definition of different colors is given in Tab. 2. The ASY-I mode with two peaks located at both sides of $\theta'=0$ mainly exist below the dash line, while the intensity distribution of the mode above the dash line has single peak pinpointed on $\theta'=0$ by the effect of saturated nonlinearity.

Table 2 Meaning of the colors in Fig. 4.

Color	Meaning
Red	Occupied only by SY
Blue	Occupied only by ASY-I
Green	Occupied only by ASY-II
Pink	Overlapped by SY and ASY-I
Yellow	Overlapped by SY and ASY-II
Purple	Overlapped by ASY-I and ASY-II
Dark gray	Overlapped by SY, ASY-I and ASY-II

of the ASY-II mode in Fig. 4, we can conclude that the nonlinear potential contributes more to the survival of the modes with nonbilateral symmetry (the ASY-I and ASY-II modes).

Some results should be noted. First, there are two types of ASY-I mode. The dashed line in Fig. 4 separates these two types. The type with two peaks located on both sides of $\theta'=0$ exists only below the dashed line, whereas that with a single peak located at $\theta'=0$ owing to the effect of saturated nonlinearity appears solely above the dashed line (the result can be seen clearly in Fig. 3). Second, by examining the distribution of stable fundamental modes in Fig. 4, we can see that the ASY-II mode is distributed mainly in the lower-energy area, whereas the ASY-I mode is located chiefly in the high-energy area. Finally, as the total power P increases, the stable ASY-I mode recovers to the SY mode. This phenomenon does not appear in the system with a Kerr nonlinearity and is called symmetry recovery. (A similar symmetry-restoration mechanism was demonstrated earlier in a system with cubic-quintic nonlinearity [48].) Because of the effect of saturated nonlinearity, high energy neutralizes the nonlinear effect, and the SY mode recovers in the region where the total power is higher than that of the counterpart in the ASY-I mode. Thus, the SY mode is distributed in both the lower- and higher-energy areas.

To investigate the symmetry breaking and symmetry recovery between these modes more clearly, we define the following two characteristics:

$$ASP_1=\left|\int_{-\pi}^{-\pi/2}|\psi(\theta')|^2\mathrm{d}\theta'+\int_{\pi/2}^{\pi}|\psi(\theta')|^2\mathrm{d}\theta'-\int_{-\pi/2}^{\pi/2}|\psi(\theta')|^2\mathrm{d}\theta'\right|/P, \tag{9}$$

$$ASP_2=\left|\int_{-\pi}^{0}|\psi(\theta')|^2\mathrm{d}\theta'-\int_{0}^{\pi}|\psi(\theta')|^2\mathrm{d}\theta'\right|/P, \tag{10}$$

which can be used to identify symmetry transitions between the SY, ASY-I, and ASY-II modes. As shown in Fig. 1(b), ASP_1 is actually used to exhibit the difference in the power on either side of the y axis, whereas ASP_2 is set to show the difference in the power on either side of the x axis.

Note that all three of these modes are generated using the same set of parameters, which implies that tristability of these modes exists in the system. Taking Fig. 4(c) for example, the SY, ASY-I, and ASY-II modes all coexist in some regions. Symmetry breaking and symmetry recovery begin at around $\omega=0.1$. The mode transition can be seen more clearly in Fig. 5. The case of $\omega=0.15$ in Figs. 5(a) and (b) shows that the first symmetry breaking occurs from the SY mode to the ASY-II mode with increasing total power P. After recovery back to the SY mode, the second symmetry breaking occurs, changing the mode from SY to ASY-I, and finally symmetry recovery occurs again, with the mode transforming from the ASY-I mode to the SY mode. For $\omega=0.2$ [shown in Figs. 5(c) and (d)], the processes of symmetry breaking from the SY mode to the ASY-II mode and symmetry recovery from the ASY-I mode to the SY mode are similar to those for $\omega=0.15$, but there is no SY mode between these two transition points. Instead, a second symmetry breaking from the ASY-II mode to the ASY-I mode occurs directly after the first symmetry breaking. The bifurcation diagram, shown in terms of ASP_1 and ASP_2, demonstrates that symmetry breaking and symmetry recovery in these cases are supercritical, that is, that no two of these stable fundamental modes can survive together. However, for $\omega=0.3$, symmetry breaking and symmetry recovery become subcritical. The branches of the stable SY, ASY-I, and ASY-II modes overlap in this case, which can be seen clearly in Figs. 5(e) and (f).

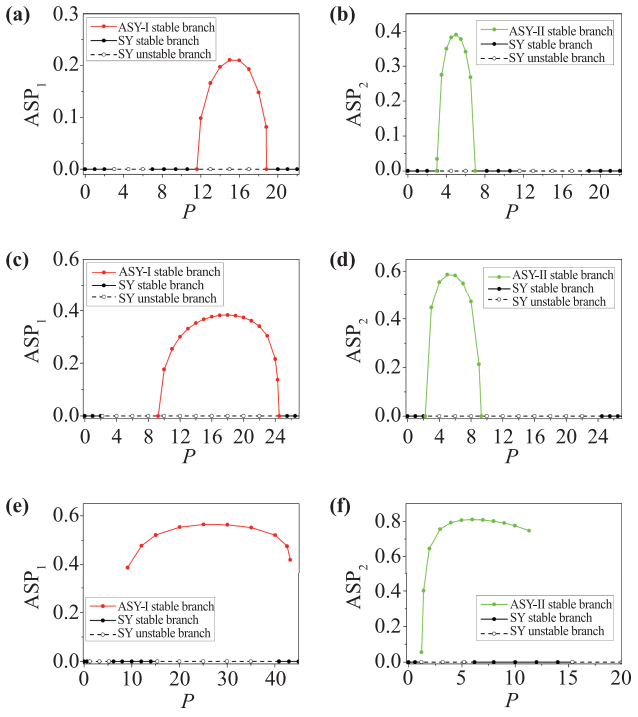

Fig. 5 Bifurcation diagram of ASP_1 and ASP_2. The set of parameters (A, ω) in panels **(a, b)**, panels **(c, d)** and panels **(e, f)** are $(2, 0.15)$, $(2, 0.2)$ and $(2, 0.3)$, respectively. Panels (a)–(d) are supercritical, while panels **(e, f)** are subcritical.

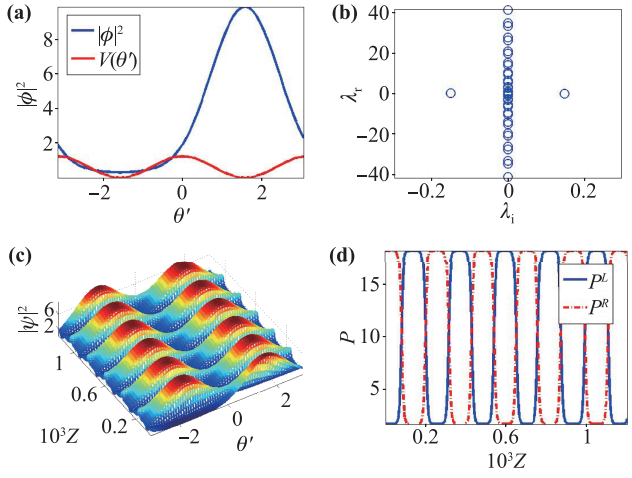

Fig. 6 **(a)** The intensity profile of an unstable ASY-II mode with a set of parameters $(A, P, \omega) = (2, 22, 0.4)$. **(b)** The growth rate of this mode. **(c)** Direct simulation of this mode. **(d)** The corresponding evolution of half-power with $P^L = \int_{-\pi}^{0} |\psi(\theta')|^2 \mathrm{d}\theta'$ and $P^R = \int_{0}^{\pi} |\psi(\theta')|^2 \mathrm{d}\theta'$.

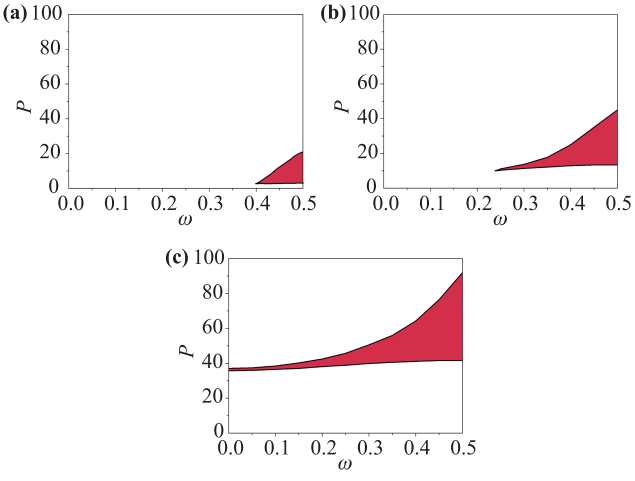

Fig. 7 The distribution regions of unstable mode in the (P, ω) plane with **(a)** $A = 1$, **(b)** $A = 2$ and **(c)** $A = 4$.

A similar system with cubic nonlinearity was studied earlier, and symmetry breaking was also considered [38]. Because the saturable nonlinear potential can be approximately equal to the combination of both the linear and cubic nonlinear potentials in the region with lower energy, as mentioned above, it would clearly be interesting to compare the picture of symmetry-breaking bifurcations obtained in our model with its counterpart studied earlier in that similar system with cubic nonlinearity. We find that the two systems have a similar dynamic of mode transition when ω is around 0.5; however, they differ when ω is close to 0. In the region of lower rotation speed, the former system does not have symmetry breaking, but the latter one always has. Thus, the symmetry-breaking scenario is not the same in these two systems.

A more detailed numerical simulation shows that a specific type of unstable ASY-II mode exists near the region of the stable ASY-II mode. Its real-time evolution features Josephson oscillation between the left and right sides of $\theta' = 0$ [shown in Figs. 6(c) and (d)] [49–53]. The distribution region of this type of mode with different amplitudes A is also calculated and is shown in Fig. 7.

As mentioned above, the model considered here is also suitable for a BEC loaded into a toroidal trap. There are also three types of corresponding stable fundamental modes found in this BEC system, which characterize a specific density distribution of the BEC atoms around the trap. These stable modes can survive together in some common region of the (P, ω) plane for a suitable value of A (e.g., $A = 2$). It would clearly be interesting to identify which mode is most stable. Thus, one horizontal line segment with parameters $(A, P) = (2, 10)$ and $0 \leq \omega \leq 0.5$ is selected to pass through the common region, and the chemical potential of the SY, ASY-I, and ASY-II modes within the line segment is determined, as shown in Fig. 8. We can easily conclude that

$$\mu_{ASY-I} < \mu_{SY} / \mu_{ASY-II}, \tag{11}$$

which clearly demonstrates that the ASY-I mode is the

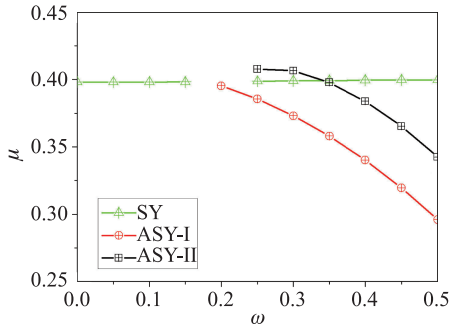

Fig. 8 The relation between chemical potential μ and rotating speed ω for all of these three types of modes in the same parameters of $(A, P) = (2, 10)$.

ground state and should be the most stable among these three types of modes.

4 Conclusion

This work studied the existence and stability of and transitions between several fundamental modes in a rotating waveguide pipe with an inverted saturated nonlinear double-well potential. The solutions of these fundamental modes were obtained using the ITP method, and the stability of the solutions was analyzed by computing the eigenvalues for small perturbations and verified by real-time simulation. This model can be realized by an air-core twisted cylindrical optical waveguide involving linear and nonlinear components of the saturated nonlinear potential with π-out-of-phase modulation. In the temporal domain, we can build a BEC loaded into a toroidal trap and establish a corresponding saturated nonlinear potential under a combination of extra optical and magnetic effects. In this model, three types of fundamental modes were found: the symmetric mode (SY mode), asymmetric mode I (ASY-I mode), and asymmetric mode II (ASY-II mode). To discuss the characteristics of these modes, the azimuthal domain of the ring is divided into four parts, two linear segments and two nonlinear segments, by the saturated nonlinear potential, defined as $\sigma V(\theta - \omega z)/(1 + |\psi|^2)$. The SY mode has double peaks located separately at the center of two linear segments. The ASY-II mode is a single-peak mode, in which the peak is located at the center of either linear segment. The ASY-I mode, however, is a specific structure with one or two peaks located somewhere in the center of one nonlinear segment. Symmetry breaking, symmetry recovery, and transitions among these three modes are greatly influenced by the amplitude of the nonlinear potential, A, and the rotation speed ω. For small values of A, symmetry breaking occurs only between the SY and ASY-I modes, whereas for large values of A, symmetry breaking occurs not only between the SY and ASY-I modes but also between the SY and ASY-II modes. Because the nonlinear potential is a type of saturated potential, the ASY-I mode can transform back to the SY mode if the total power is large enough, which is called symmetry recovery. Moreover, detailed examination revealed a specific type of unstable ASY-II mode. The real-time evolution of the unstable ASY-II mode is characterized by Josephson oscillation between two linear potential wells, and the distribution regions of the unstable ASY-II mode are also depicted for certain values of A. Finally, by considering a model suitable for BECs, the ASY-I mode is identified as the ground state mode.

An interesting extension of this work may be to consider a rotating nonlocal nonlinear potential, such as setting dipolar BECs in a rotating trap, which possesses long-range dipole-dipole interactions [54–60] or quadrupole-quadrupole interactions [61–63]. Another extension is to consider this model in a discrete form [64–66, 68–75] and to investigate the optical field transmission across a bunch of twisted waveguide pipes.

Acknowledgements G. Chen appreciates the useful discussions with Yongyao Li (SCAU Univ.). This work was supported by the National Natural Science Foundation of China (Grant No. 61308019), Guangdong Natural Science Foundation (Grant No. 2015A030313650), and the Foundation for Distinguished Young Talents in Higher Education of Guangdong (Grant No. Yq2013157).

References

1. Q. Gong and X. Hu, Ultrafast photonic crystal optical switching, *Front. Phys.* 1, 171 (2006)
2. Y. Liu, F. Qin, F. Zhou, Q. Meng, D. Zhang, and Z. Li, Ultrafast optical switching in Kerr nonlinear photonic crystals, *Front. Phys.* 5, 244 (2010)
3. M. Shen, B. Li, L. Ge, W. Chen, and D. Wu, Stability of vortex solitons under competing local and nonlocal cubic nonlinearities, *Opt. Commun.* 338, 27 (2015)
4. Y. J. Xiang, X. Y. Dai, S. C. Wen, and D. Y. Fan, Modulation instability in metamaterials with saturable nonlinearity, *J. Opt. Soc. Am. B* 28(4), 908 (2011)
5. T. R. O. Melvin, A. R. Champneys, P. G. Kevrekidis, and J. Cuevas, Travelling solitary waves in the discrete Schrodinger equation with saturable nonlinearity: Existence, stability and dynamics, *Physica D* 237(4), 551 (2008)
6. F. Setzpfandt, A. A. Sukhorukov, and T. Pertsch, Discrete quadratic solitons with competing second-harmonic components, *Phys. Rev. A* 84(5), 053843 (2011)

7. V. Lutsky and B. A. Malomed, One- and two-dimensional solitons supported by singular modulation of quadratic nonlinearity, *Phys. Rev. A* 91(2), 023815 (2015)
8. M. Shen, Y. Y. Lin, C. C. Jeng, and R. K. Lee, Vortex pairs in nonlocal nonlinear media, *J. Opt.* 14(6), 065204 (2012)
9. M. Shen, J. S. Gao, and L. J. Ge, Solitons shedding from Airy beams and bound states of breathing Airy solitons in nonlocal nonlinear media, *Sci. Rep.* 5, 9814 (2015)
10. Y. V. Kartashov, B. A. Malomed, and L. Torner, Solitons in nonlinear lattices, *Rev. Mod. Phys.* 83(1), 247 (2011)
11. Y. S. Kivshar, Nonlinear Tamm states and surface effects in periodic photonic structures, *Laser Phys. Lett.* 5(10), 703 (2008)
12. Y. V. Kartashov, A. Ferrando, A. A. Egorov, and L. Torner, Soliton topology versus discrete symmetry in optical lattices, *Phys. Rev. Lett.* 95(12), 123902 (2005)
13. Y. Li, W. Pang, Y. Chen, Z. Yu, J. Zhou, and H. Zhang, Defect-mediated discrete solitons in optically induced photorefractive lattices, *Phys. Rev. A* 80(4), 043824 (2009)
14. W. M. Liu, B. Wu, and Q. Niu, Nonlinear effects in interference of Bose–Einstein condensates, *Phys. Rev. Lett.* 84(11), 2294 (2000)
15. Z. X. Liang, Z. D. Zhang, and W. M. Liu, Dynamics of a bright soliton in Bose–Einstein condensates with time-dependent atomic scattering length in an expulsive parabolic potential, *Phys. Rev. Lett.* 94(5), 050402 (2005)
16. A. C. Ji, W. M. Liu, J. L. Song, and F. Zhou, Dynamical creation of fractionalized vortices and vortex lattices, *Phys. Rev. Lett.* 101(1), 010402 (2008)
17. E. A. Ostrovskaya and Y. S. Kivshar, Matter-wave gap solitons in atomic band-gap structures, *Phys. Rev. Lett.* 90(16), 160407 (2003)
18. N. K. Efremidis and D. N. Christodoulides, Lattice solitons in Bose–Einstein condensates, *Phys. Rev. A* 67(6), 063608 (2003)
19. H. Sakaguchi and B. A. Malomed, Matter-wave solitons in nonlinear optical lattices, *Phys. Rev. E* 72(4), 046610 (2005)
20. B. B. Baizakov, B. A. Malomed, and M. Salerno, Matterwave solitons in radially periodic potentials, *Phys. Rev. E* 74(6), 066615 (2006)
21. O. Morsch and M. Oberthaler, Dynamics of Bose–Einstein condensates in optical lattices, *Rev. Mod. Phys.* 78(1), 179 (2006)
22. H. Sakaguchi and B. A. Malomed, Solitons in combined linear and nonlinear lattice potentials, *Phys. Rev. A* 81(1), 013624 (2010)
23. Y. Li, B. A. Malomed, M. Feng, and J. Zhou, Double symmetry breaking of solitons in one-dimensional virtual photonic crystals, *Phys. Rev. A* 83(5), 053832 (2011)
24. Y. Li, B. A. Malomed, J. Wu, W. Pang, S. Wang, and J. Zhou, Quasicompactons in inverted nonlinear photonic crystals, *Phys. Rev. A* 84(4), 043839 (2011)
25. Y. Li, W. Pang, S. Fu, and B. A. Malomed, Twocomponent solitons with a spatially modulated linear coupling: Inverted photonic crystals and fused couplers, *Phys. Rev. A* 85(5), 053821 (2012)
26. G. Chen, S. Zhang, and M. Wu, Optical solitons in a trinal-chennel inverted nonlinear photonic crystal, *J. Nonlinear Opt. Phys. Mater.* 22(01), 1350012 (2013)
27. W. Pang, H. Guo, G. Chen, and Z. Mai, Symmetry breaking bifurcation of two-component soliton modes in an inverted nonlinear random lattice, *J. Phys. Soc. Jpn.* 83(3), 034402 (2014)
28. J. Deng, J. Liu, S. Tan, Z. Huang, and Y. Li, Propagation dynamic of a Gaussian in the inverted nonlinear photonic crystals, *Optik (Stuttg.)* 125(15), 4088 (2014)
29. H. Guo, Z. Chen, J. Liu, and Y. Li, Fundamental modes in a waveguide pipe twisted by inverted nonlinear doublewell potential, *Laser Phys.* 24(4), 045403 (2014)
30. A. Szameit, J. Burghoff, T. Pertsch, S. Nolte, A. Tünnermann, and F. Lederer, Two-dimensional soliton in cubic fs laser written waveguide arrays in fused silica, *Opt. Express* 14(13), 6055 (2006)
31. D. Blömer, A. Szameit, F. Dreisow, T. Schreiber, S. Nolte, and A. Tünnermann, Nonlinear refractive index of fs-laser-written waveguides in fused silica, *Opt. Express* 14(6), 2151 (2006)
32. Y. Li, B. A. Malomed, M. Feng, and J. Zhou, Arrayed and checkerboard optical waveguides controlled by the electromagnetically induced transparency, *Phys. Rev. A* 82(6), 063813 (2010)
33. J. Wu, M. Feng, W. Pang, S. Fu, and Y. Li, The transmission of quasi-discrete solitons in resonant waveguide arrays activated by the electromagnetically induced transparency, *J. Nonlinear Opt. Phys. Mater.* 20(02), 193 (2011)
34. W. Pang, J. Wu, Z. Yuan, Y. Liu, and G. Chen, Lattice solitons in optical lattice controlled by electromagnetically induced transparency, *J. Phys. Soc. Jpn.* 80(11), 113401 (2011)
35. H. Saito and M. Ueda, Emergence of Bloch bands in a rotating Bose–Einstein condensate, *Phys. Rev. Lett.* 93(22), 220402 (2004)
36. S. Schwartz, M. Cozzini, C. Menotti, I. Carusotto, P. Bouyer, and S. Stringari, One-dimensional description of a Bose–Einstein condensate in a rotating closed-loop waveguide, *New J. Phys.* 8(8), 162 (2006)
37. L. Wen, H. Xiong, and B. Wu, Hidden vortices in a Bose–Einstein condensate in a rotating double-well potential, *Phys. Rev. A* 82(5), 053627 (2010)

38. Y. Li, W. Pang, and B. A. Malomed, Nonlinear modes and symmetry breaking in rotating double-well potentials, *Phys. Rev. A* 86(2), 023832 (2012)
39. G. Chen, Z. Luo, J. Wu, and M. Wu, Switch between the types of the symmetry breaking bifurcation in optically induced photorefractive rotational double-well potential, *J. Phys. Soc. Jpn.* 82(3), 034401 (2013)
40. Z. Luo, Y. Li, W. Pang, Y. Liu, and X. Wang, Double symmetry breaking of modes in dual-core rotating system, *J. Phys. Soc. Jpn.* 82(12), 124401 (2013)
41. W. Pang, S. Fu, J. Wu, Y. Li, and Z. Mai, Nonlinear mode in rotating double-well potential with parity-time symmetry, *Chin. Phys. B* 23(10), 104214 (2014)
42. J. Li, B. Liang, Y. Liu, P. Zhang, J. Zhou, S. O. Klimonsky, A. S. Slesarev, Y. D. Tretyakov, L. O'Faolain, and T. F. Krauss, Photonic crystal formed by the imaginary part of the refractive index, *Adv. Mater.* 22(24), 2676 (2010)
43. M. Feng, Y. Liu, Y. Li, X. Xie, and J. Zhou, Light propagation in a resonantly absorbing waveguide array, *Opt. Express* 19(8), 7222 (2011)
44. B. Liang, Y. Liu, J. Li, L. Song, Y. Li, J. Zhou, and K. S. Wong, Frabication of large-size photonic crystals by holographic lithography using a lens array, *J. Micromech. Microeng.* 22(3), 035013 (2012)
45. Y. K. Liu, S. C. Wang, Y. Y. Li, L. Y. Song, X. S. Xie, M. N. Feng, Z. M. Xiao, S. Z. Deng, J. Y. Zhou, J. T. Li, K. Sing Wong, and T. F. Krauss, Effcient color routing with a dispersion-controlled waveguide array, *Light Sci. Appl.* 2(2), e52 (2013)
46. L. M. Chiofalo, S. Succi, and P. M. Tosi, Ground state of trapped interacting Bose–Einstein condensates by an explicit imaginarytime algorithm, *Phys. Rev. E Stat. Phys. Plasmas Fluids Relat. Interdiscip. Topics* 62(5), 7438 (2000)
47. J. Yang and T. I. Lakoba, Accelerated imaginary-time evolution methods for the computation of solitary waves, *Stud. Appl. Math.* 120(3), 265 (2008)
48. L. Albuch and B. A. Malomed, Transitions between symmetric and asymmetric solitons in dual-core systems with cubicquintic nonlinearity, *Math. Comput. Simul.* 74(4-5), 312 (2007)
49. G. Mazzarella and L. Salasnich, Spontaneous symmetry breaking and collapse in bosonic Josephson junctions, *Phys. Rev. A* 82(3), 033611 (2010)
50. L. K. Lim, T. Troppenz, and C. M. Smith, Internal Josephson oscillations for distinct momenta Bose–Einstein condensates, *Phys. Rev. A* 84(5), 053609 (2011)
51. J. Gillet, M. A. Garcia-March, T. Busch, and F. Sols, Tunneling, self-trapping, and manipulation of higher modes of a Bose–Einstein condensate in a double well, *Phys. Rev. A* 89, 023614 (2014)
52. G. Szirmai, G. Mazzarella, and L. Salasnich, Tunneling dynamics of bosonic Josephson junctions assisted by a cavity field, *Phys. Rev. A* 91(2), 023601 (2015)
53. J. Javanainen and R. Rajapakse, Bayesian inference to characterize Josephson oscillations in a double-well trap, *Phys. Rev. A* 92, 023613 (2015)
54. P. Pedri and L. Santos, Two-dimensional bright solitons in dipolar Bose–Einstein condensates, *Phys. Rev. Lett.* 95(20), 200404 (2005)
55. R. Nath, P. Pedri, and L. Santos, Stability of dark solitons in three dimensional dipolar Bose–Einstein condensates, *Phys. Rev. Lett.* 101(21), 210402 (2008)
56. I. Tikhonenkov, B. A. Malomed, and A. Vardi, Vortex solitons in dipolar Bose–Einstein condensates, *Phys. Rev. A* 78(4), 043614 (2008)
57. Y. Li, J. Liu, W. Pang, and B. A. Malomed, Matter-wave solitons supported by field-induced dipole-dipole repulsion with spatially modulated strength, *Phys. Rev. A* 88(5), 053630 (2013)
58. I. Tikhonenkov, B. A. Malomed, and A. Vardi, Anisotropic solitons in dipolar Bose–Einstein condensates, *Phys. Rev. Lett.* 100(9), 090406 (2008)
59. S. K. Adhikari, Self-trapping of a dipolar Bose–Einstein condensate in a double well, *Phys. Rev. A* 89(4), 043609 (2014)
60. X. Jiang, Z. Fan, Z. Chen, W. Pang, Y. Li, and B. A. Malomed, Two-dimensional solitons in dipolar Bose–Einstein condensates with spin-orbit coupling, *Phys. Rev. A* 93(2), 023633 (2016)
61. J. M. Junquera-Hernández, J. Sánchez-Marín, and D. Maynau, Molecular electric quadrupole moments calculated with matrix dressed SDCI, *Chem. Phys. Lett.* 359(3-4), 343 (2002)
62. Y. Li, J. Liu, W. Pang, and B. A. Malomed, Lattice solitons with quadrupolar intersite interactions, *Phys. Rev. A* 88(6), 063635 (2013)
63. J. Huang, X. Jiang, H. Chen, Z. Fan, W. Pang, and Y. Li, Quadrupolar matter-wave soliton in two-dimensional free space, *Front. Phys.* 10(4), 100507 (2015)
64. D. N. Christodoulides, F. Lederer, and Y. Silberberg, Discretizing light behaviour in linear and nonlinear waveguide lattices, *Nature* 424(6950), 817 (2003)
65. F. Lederer, G. I. Stegeman, D. N. Christodoulides, G. Assanto, M. Segev, and Y. Silberberg, Discrete solitons in optics, *Phys. Rep.* 463(1-3), 1 (2008)
66. S. Flach and A. V. Gorbach, Discrete breathers Advances in theory and applications, *Phys. Rep.* 467(1-3), 1 (2008)
67. X. Zhang, J. Chai, J. Huang, Z. Chen, Y. Li, and B. A. Malomed, Discrete solitons and scattering of lattice wave in guiding arrays with a nonlinear PT-symmetric defect, *Opt. Express* 22(11), 13927 (2014)
68. Z. Chen, J. Liu, S. Fu, Y. Li, and B. A. Malomed, Discrete solitons and vortices on two-dimensional lattices of PT-symmetric couplers, *Opt. Express* 22(24), 29679 (2014)

69. G. Chen, H. Huang, and M. Wu, Solitary vortices in two dimensional waveguide matrix, *J. Nonlinear Opt. Phys. Mater.* 24(01), 1550012 (2015)

70. Z. Mai, S. Fu, J. Wu, and Y. Li, Discrete soliton in waveguide arrays with long-range linearly coupled effect, *J. Phys. Soc. Jpn.* 83(3), 034404 (2014)

71. Z. Mai, W. Pang, J. Wu, and Y. Li, Symmetry breaking of discrete solitons in two-component waveguide arrays with long-range linearly coupled effect, *J. Phys. Soc. Jpn.* 84(1), 014401 (2015)

72. J. Huang, H. Li, X. Zhang, and Y. Li, Transmission, reflection, scattering, and trapping of traveling discrete solitons by C and V point defects, *Front. Phys.* 10(2), 104201 (2015)

73. Z. Chen, J. Huang, J. Chai, X. Zhang, Y. Li, and B. A. Malomed, Discrete solitons in self-defocusing systems with PT-symmetric defects, *Phys. Rev. A* 91(5), 053821 (2015)

74. U. Al Khawaja, and A. A. Sukhorukov, Unidirectional ow of discrete solitons in waveguide arrays, *Opt. Lett.* 40(12), 2719 (2015)

75. Z. Peng, H. Li, Z. Fan, X. Zhang, and Y. Li, All optical diode realized by one dimensional waveguide array, *J. Nonlinear Opt. Phys. Mater.* 24(02), 1550022 (2015)